UNDERSTANDING HYDROMETEOROLOGY USING GLOBAL MODELS

BY ALAN K. BETTS*

A new framework is proposed for understanding the land surface coupling in global models between soil moisture, cloud base and cloud cover, the radiation fields, the surface energy partition, evaporation, and precipitation.

UNDERSTANDING THE CLIMATE OVER LAND. The title of this paper is meant to be a paradox. Usually we rely on simple models to gain understanding, but hydrometeorology is too complex for that, and too important for us to be satisfied with rough approximations. The climate interactions of water (vapor, liquid and ice, and its phase change and radiation interactions) are everywhere, and they are central to and closely coupled to life, and to understanding climate change. The energy and water balance over land in the climate system matters critically to our civilization, and we have to face this fact. Climate is both local and global: we need earth system models to understand the coupled system that we observe, and we need them to tell us, for example, the local diurnal cycle in September, to warn us of the first frost. Only with models can we try to both fit the parts together, and then take them apart again to see what matters, and where. It is true that global models are such a challenge to construct, code, and debug; that when they run, producing something closely resembling the climate of the earth, the temptation is to sit back with relief. We run ensembles for weather forecasting and climate scenarios, talk about the complexities of cloud feedback and publish papers, and forward the results to the public and those in power to address questions of pressing political importance. But, we have to do much better—we must understand how well the models represent physical processes and feedbacks.

After a couple of decades of studying convection in the Tropics, moist thermodynamics, and climate using simple models, I realized about 15 years ago that *improving our global models* was essential to understanding the earth system. I have spent considerable effort since evaluating global models using high-quality field data (Betts et al. 1996), primarily over land from land surface experiments such as the First International Satellite Land Surface Climatology Project (ISLSCP) Field Experiment (FIFE), Boreal Ecosystem–Atmosphere Study (BOREAS), and Large-Scale Biosphere–Atmosphere Experiment

*Alan K. Betts was named the 2004 Robert E. Horton Lecturer in Hydrology. This paper was presented in a session sponsored by the 18th Conference on Hydrology at the 84th AMS Annual Meeting, January 2004.

AFFILIATIONS: BETTS—Atmospheric Research, Pittsford, Vermont
CORRESPONDING AUTHOR: Alan K. Betts, Atmospheric Research, Pittsford, VT 05763
E-mail: akbetts@aol.com
DOI:10.1175/BAMS-85-11-1673

In final form 30 April 2004

(LBA), and it is this that drew me into hydrometeorology. Along the way, however, I have realized that global models can be used as tools to understand interacting processes—the theme of this discussion. Using global models in this way is also useful, because it forces us to contrast *our model world,* which we dimly understand because at least we wrote the equations, with the *real world,* where we only understand fragments of a complex living system. Simple models are always interesting for comparison, but if you have thrown out some of the key physics (as often happens), they may not be very useful.

One way to encapsulate "hydrometeorology" is to ask what controls evapotranspiration, or to consider the classic problem of "*equilibrium evaporation.*" This has a long history (see recent reviews by Raupach 2000, 2001). Equilibrium evaporation models in their most recent formulation are models for the growing daytime "dry" boundary layer (BL), even though they deal with surface evaporation. The solutions are fascinating, but this is an excellent example of simplifying by ignoring some of the key physics, which control evaporation in the real world for climate equilibrium. *What is this ignored physics?*

a) The cloud fields "control" cloud base, the surface net radiation, and the diabatic processes in the convective BL, which means that the dry BL solutions are inadequate.
b) The climate problem is a 24-h mean problem, with a superimposed diurnal cycle, which means that it is not just a growing daytime BL problem.

Both of these realities impose first-order constraints on surface evapotranspiration. In global models with coupled cloud fields, these cloud- and BL-related processes are included, because they cannot be ignored. This does not mean they are necessarily represented well but, as we shall see, they can help us understand the links involved and suggest a framework for validation against data. The description of model BL climate in terms of daily means represents a major conceptual shift from a focus on modeling the growth of the daytime dry BL. It has been motivated in part by simple models for the equilibrium BL over land (Betts 2000; Betts et al. 2004). (Recall that not long ago, many climate models ignored the diurnal cycle to reduce computational cost!) However, we shall show, using the European Centre for Medium-Range Weather Forecasts (ECMWF) reanalysis data, which resolve the diurnal cycle and have a prognostic interactive cloud field, that the transitions in the BL climate over land can be mapped with remarkable precision by the daily mean state and daily flux averages.

CONTINENTAL SCALE EVAPORATION–PRECIPITATION FEEDBACK: IDEALIZED SOIL MOISTURE SIMULATIONS.

The 1993 Mississippi flood. This work began 10 yr ago with a little serendipity. The great flood on the Mississippi River of July 1993 occurred in the same month ECMWF was running in parallel its new land surface model (Viterbo and Beljaars 1995) with four soil layers to better represent soil moisture memory. This model had been developed using in part the land surface and soil moisture data from the 1987 FIFE experiment in Kansas, which I had been analyzing (Betts et al. 1993; Betts and Ball 1994, 1995). The 10-day forecasts with the new four-soil-layer model were much better for the July 1993 rainfall than the old two-layer model, which naturally then became history. After watching the catastrophic flood, I called up Martin Miller at ECMWF one Friday (I think in early August) and suggested running soil moisture sensitivity experiments for July 1993. We had seen considerable sensitivity in idealized seasonal soil moisture experiments. Forecasts starting in May with wet or dry soils showed a significant positive feedback on precipitation over the summer. By Monday, the forecasts and diagnostics had been run, and Martin Miller called with some excitement when he saw the results shown in Fig. 1. The difference in the total July precipitation between forecasts starting with wet or dry initial soil conditions on 1 July peaked at over 4 mm day^{-1} (red-shaded contours), corresponding to >120 mm for the month, located close to the observed precipitation maximum over the central United States. A talk on this was given at the 1994 Nashville, Tennessee, meeting of the American Meteorological Society, which was later extended for publication (Beljaars et al. 1996). It is clear that the positive feedback on precipitation is large in the model if the soil is initially wet (we shall define exactly how soil water was specified in a moment), and this positive signal can be seen over most of the continental United States. Locally, one difference we noticed was that the cloud base was much lower over initially wet soils.

Seasonal forecasts with idealized soil moisture. We shall now revisit this issue globally over land with the model used for the recent ECMWF 40-yr reanalysis (ERA-40), which has a more recent land surface model, including a distribution of vegetation types (Van den Hurk et al. 2000) and other revisions to the physics, and will try to understand the processes involved. Now "understand" in the context of a global model means to understand the links between the many coupled processes, and try to pick out the observables that can be tested against real data. (This task will, however, be left for later work.) I do not need to remind you that even the best of our models of the world are virtual realities. They are very useful though, because it is the interactions between processes that produce our interesting weather and climate, and only by exploring what models show and where they fail, can we produce better models.

We shall compare precipitation P, evaporation E, the difference thereof (P–E), which is a measure of the atmospheric convergence of water vapor, and a soil moisture index in two 120-day forecasts from 1 May 1987 using the ERA-40 forecast model, run at a resolution of T-95 L60 (triangular spectral truncation of T-95, with 60 model levels in the vertical). These seasonal forecasts have identical sea surface temperatures and initial conditions, except for initial soil moisture. One wet forecast has soil moisture initialized at 100% of field capacity for vegetated areas, and the dry forecast is initialized with soil moisture at 25% of "soil moisture availability" for vegetated areas. This soil moisture availability is the water storage between the model permanent wilting point (PWP) and the field capacity (FC). The closely related soil moisture index (SMI) is scaled by this availability, so that 0 < SMI < 1 as PWP < soil moisture < FC. The next few figures compare these forecasts for different regions, and we show 5-day means, omitting the first 5 days of each forecast. Figure 2 is an average for the United States from 32°–50°N and 80°–110°W. The reduction of SMI halves precipitation and evaporation over the summer, and changes the time sequence of P–E. The small mean summer divergence

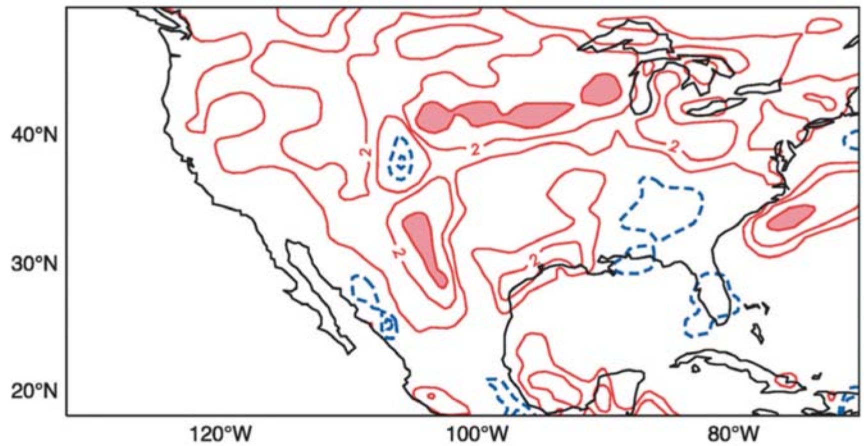

Fig. 1. Difference in the 30-day precipitation between two ensembles of three T-106 forecasts starting with wet or dry initial soil conditions on 1–3 Jul (Beljaars et al. 1996). Contours are at ±1, 2, 4 mm day^{-1}, with the +4 contour shaded red.

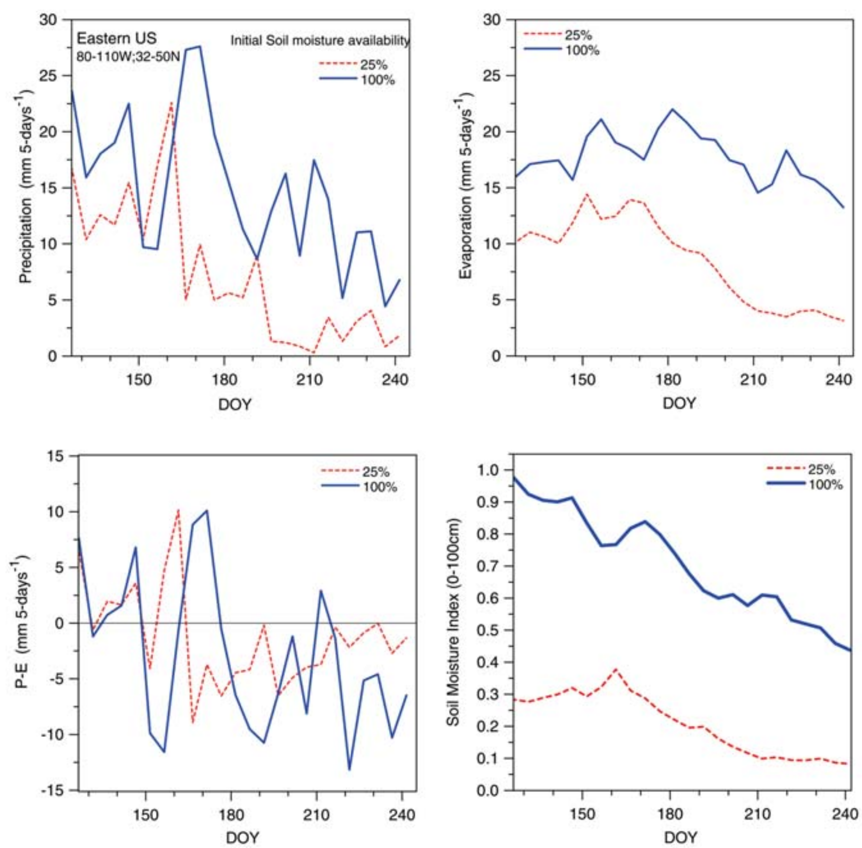

Fig. 2. The *P, E, P–E*, and soil moisture index for the eastern United States from two 120-day forecasts from 1 May 1987, starting with initial soil moisture availability of 100% and 25% for vegetated areas.

of $P–E$ (about 15% of E) is also halved. The memory of the initial soil moisture is retained throughout the summer dry down.

Figure 3 shows an average for Europe from 44°–54°N and 0°–25°E. Precipitation and vapor convergence ($P–E$) show large synoptic variability, but precipitation is reduced when evaporation is lower and mean $P–E$ remains small. The memory of the initial soil moisture is retained all summer. Similar figures for Canada and northern Asia (not shown) show the long seasonal memory of soil moisture at high latitudes. Table 1 summarizes these components of the water budget for the northern summer in this pair of forecasts for different continental regions, starting at high latitudes and ending with monsoon regions. At high latitudes, $P–E$ is a small fraction of both evaporation and precipitation, and at the end of August the difference in SMI between the two 120-day integrations remains large. For Canada and Europe, precipitation more than doubles in the wet simulation. For the United States, central Asia, and the Amazon the memory of soil moisture is significant and the initially wet simulations have roughly double the precipitation and evaporation of the dry simulations. For these three the export of water vapor ($P–E$) increases slightly in the wet simulation, so that the adjustment of the large-scale circulation reduces slightly the precipitation–evaporation feedback. The last three basins are influenced significantly by the African and Indian monsoons. There is convergence of water vapor into these regions, which, for the Indian region, contributes nearly two-thirds of the precipitation. The contribution of increased evaporation to precipitation, though visible, is, therefore, relatively smaller. At the same time the excess of precipitation over evaporation reduces the memory of soil moisture in these monsoon regions. For the Indian region the soil moisture index for the dry simulation has climbed to 0.78 from an initial value close to 0.25.

It is clear that away from the monsoons, it is evaporation that largely determines precipitation over the continents on climate time scales. Hence, we need to understand what processes are coupled to evaporation. We shall start with soil moisture.

Soil moisture, surface energy balance, and height of cloud base. First, we present scatterplots of the 5-day mean surface fluxes against soil moisture for the dry and wet initial simulations for the three regions of the Americas: Canada, the United States, and the Amazon. Figure 4 shows latent heat flux λE, sensible heat flux H, surface net radiation R_{net}, and the mean lifting condensation level (LCL) height P_{LCL} in pressure units, the mean height of the cloud base for parcels lifted from the surface, as functions of the first model soil layer (0–7 cm) SMI. Points are distinguished as W or D, according to whether they are from an initially wet or dry SMI, respectively, but we have not distinguished the three regions. Because each point is a 5-day mean, we have smoothed some of the synoptic variability. We have kept the sign convention of the global model that upward fluxes are negative. Here, R_{net} has no trend with SMI across the basins and dry or wet initial soil conditions, but the upward

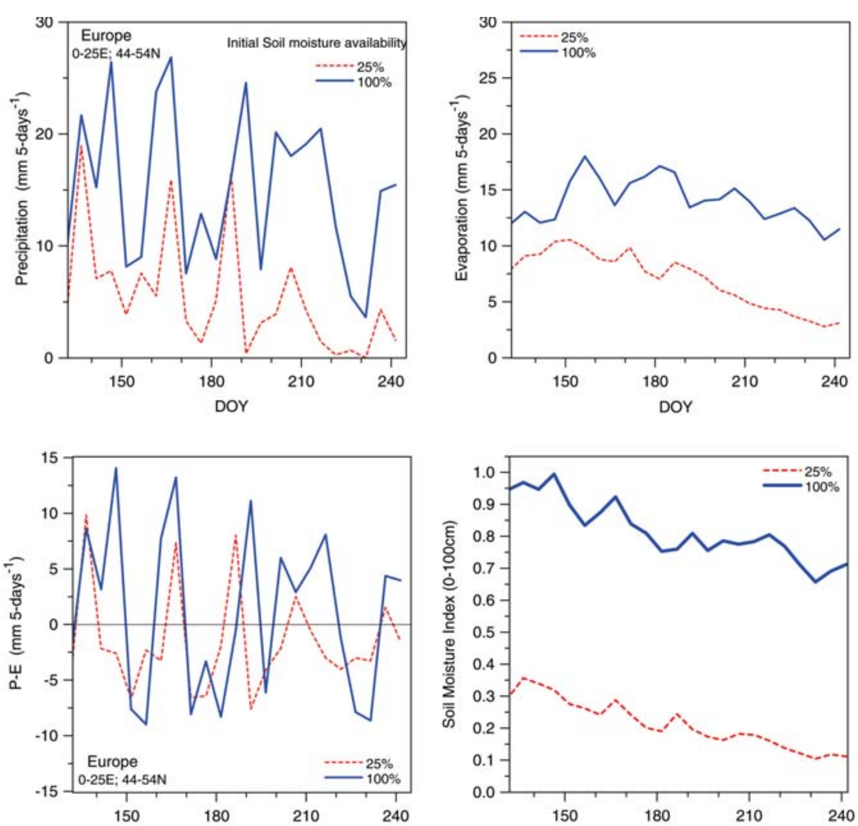

Fig. 3. As in Fig. 2, but for Europe.

Table 1. Five-day mean summer precipitation *P*, evaporation *E*, *P–E*, and end-of-Aug soil moisture index for forecasts with initial dry and wet soil moisture index.

	Precipitation (mm 5-day^{-1})		Evaporation (mm 5-day^{-1})		*P–E* (mm 5-day^{-1})		SMI (0–100 cm) day = 241.5		Diff of SMI
Initial SMI:	**Dry**	**Wet**	**Dry**	**Wet**	**Dry**	**Wet**	**Dry**	**Wet**	
Canada 50°–70°N, 130°–90°W	5.2	12.1	5.6	11.5	–0.4	0.6	0.19	0.86	0.67
North Asia 50°–70°N, 25°–140°E	6.0	11.2	5.6	10.8	0.4	0.4	0.28	0.77	0.49
Europe 44°–54°N, 0°–25°E	6.0	15.5	7.0	13.9	–1.0	1.6	0.11	0.71	0.60
United States 32°–50°N, 110°–80°W	7.3	14.8	8.6	17.6	–1.3	–2.9	0.08	0.44	0.38
Central Asia 35°–50°N, 40°–100°E	3.2	7.5	3.5	9.2	–0.3	–1.7	0.16	0.37	0.21
Amazon 5°N–10°S, 50°–70°W	4.6	11.5	6.8	14.7	–2.2	–3.2	0.04	0.27	0.23
Equatorial Africa 10°N–10°S, 14°–35°E	12.6	18.5	8.9	13.3	3.7	5.2	0.40	0.62	0.22
Africa/Sahel 10°–20°N, 15°W–40°E	14.8	18.2	7.1	10.0	7.6	8.1	0.58	0.67	0.09
India 18°–35°N, 70°–90°E	28.4	32.7	9.3	14.3	19.1	18.4	0.78	0.93	0.15

sensible heat decreases almost uniformly as SMI increases. Latent heat flux, which can be regarded as the sum $R_{net} + H$ (given our sign convention, and neglecting ground storage), does generally increase over wetter soils, but the scatter coming from the scatter in R_{net} is apparent. The lower-right panel shows one crucial link in the physics; the mean depth to the cloud base, which we can also

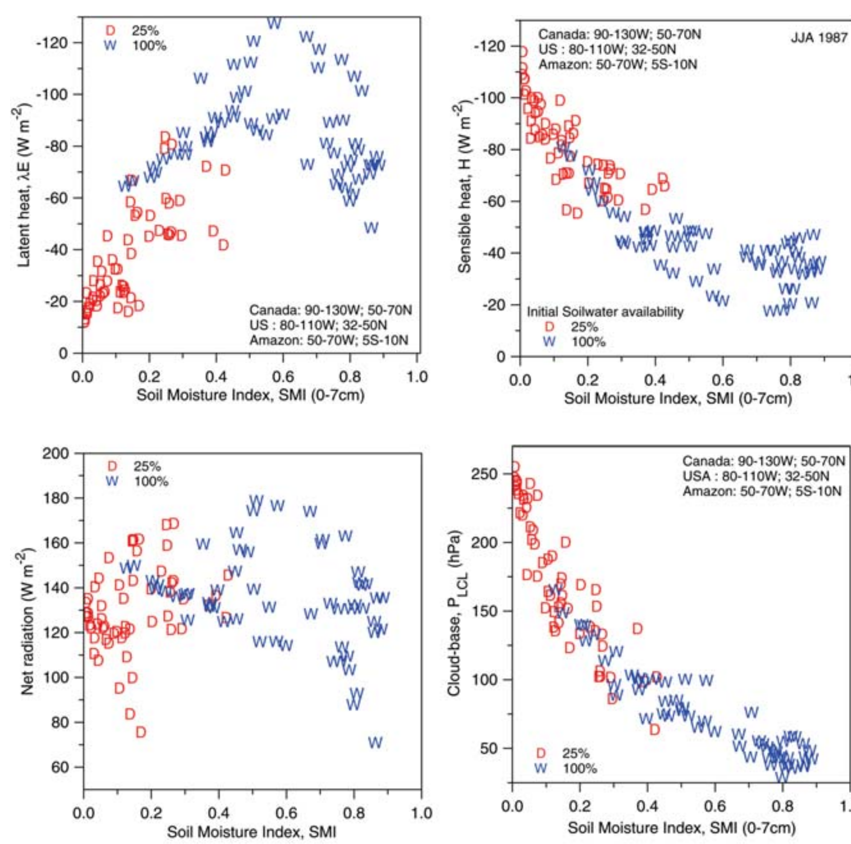

Fig. 4. Five-day mean latent heat flux λE, sensible heat flux H, surface net radiation R_{net}, and mean cloud-base height P_{LCL} in pressure units, as functions of the first model soil-layer (0–7 cm) soil moisture index.

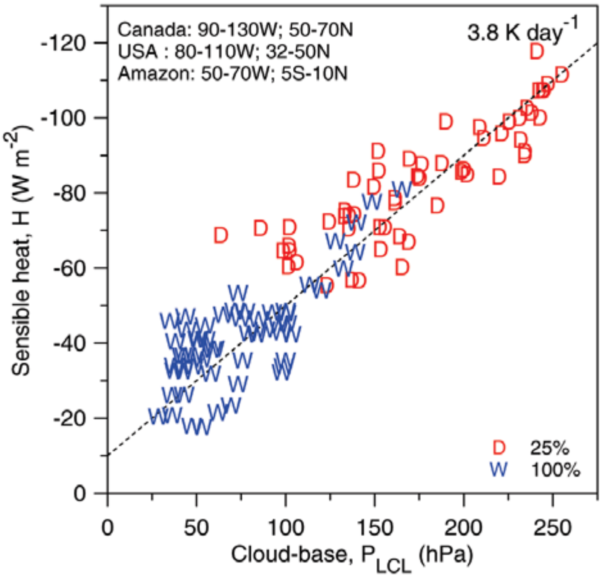

FIG. 5. Five-day mean sensible heat flux as a function of P_{LCL}.

consider the mean mixed-layer (ML) depth, has a very tight relationship to SMI (see Betts 2000; Betts et al. 2004) and spans these three large regions from the Tropics to high latitudes and both 120-day forecasts, starting from very different initial conditions.

Figure 5 shows that sensible heat flux plotted against P_{LCL} is a quasi-linear distribution with a slope corresponding to a heating rate of 3.8 K day^{-1}. On this 5-day time scale, the heating of the mixed layer by the surface flux (and the entrainment at ML top, which is modeled as a small fraction of the surface flux; Betts 1973; Beljaars and Betts 1993) closely balances the diabatic processes cooling the mixed layer, which in the model are radiative cooling and the evaporation of falling precipitation. Thus, the coupling between H and SMI is linked to the coupling of H to P_{LCL}, and P_{LCL} to SMI. On the other hand, R_{net} [the sum of net shortwave (SW_{net}) and net longwave (LW_{net}) radiation] depends on the cloud fields and the atmospheric moisture and temperature structure.

Mixed-layer "equilibrium." We now look at the Amazon region in more detail, and show how the equilibrium of the mixed layer and the surface fluxes both change as mean cloud base changes during the integrations. Figure 6 has two panels: on the left is sensible heat flux (with label H) and latent heat flux (with label E) as a function of cloud-base P_{LCL}. The points are again 5-day means of both 120-day forecasts, but we do not distinguish which points were from the initially dry or wet soil moisture, because the distributions merge. With a deeper mean cloud base, H is larger and λE is smaller, and both distributions are quasi linear. The panel on the right shows how the 5-day mean 2-m temperature (labeled T) increases and 2-m mixing ratio (labeled Q) decreases as P_{LCL} increases. The dashed lines on both panels are the corresponding fluxes, temperature, and mixing ratio from the idealized equilibrium ML solutions of Betts et al. (2004), with parameters roughly fitted to the Amazon. Recalling that Fig. 4 showed the tight link between SMI and P_{LCL}, it is clear that what we are seeing is the shift in the equilibrium of the ML and the surface fluxes as soil moisture changes. Over wetter soils, cloud base is lower with a cooler, moister ML, larger λE, and smaller H. The fact that there is general agreement between the Amazon 5-day means taken from the pair of 120-day forecasts with the idealized equilibrium model of Betts et al. (2004) suggests that this aspect of the coupled system can be understood with a simplified diurnally averaged model.

LAND SURFACE COUPLING AT DAILY TIME SCALE.

To better understand the coupling of soil moisture, cloud base, cloud cover, the radiation fields, the sensible and latent heat fluxes, and the diurnal cycle, we are going to drop down to the daily time scale, and use 30 yr of daily river basin data from ERA-40.

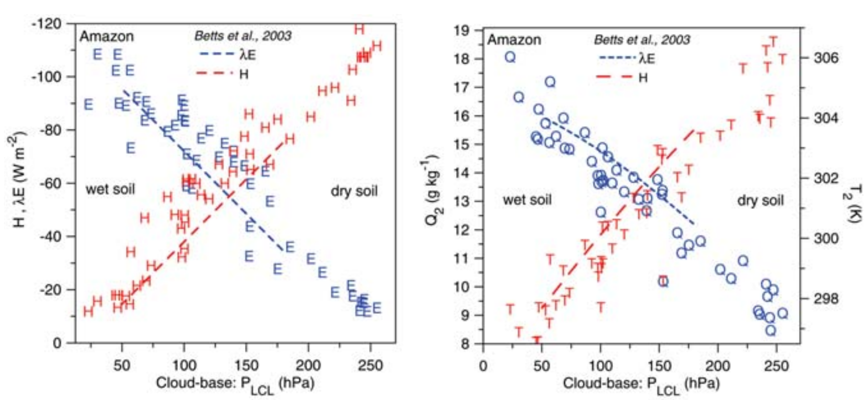

FIG. 6. 5-day mean sensible heat flux (labeled *H*) and latent heat flux (labeled *E*) as a function of (left) cloud base P_{LCL} and (right) 5-day mean 2-m temperature (labeled *T*) and 2-m mixing ratio (labeled Q) as a function of P_{LCL}. Dashed lines are idealized model solution.

ERA-40 river basin budgets. The research archive from ERA-40 contains an hourly time series, averaged over selected river basins (with the fluxes integrated from the full time resolution of the model). These have been used to assess the biases of ERA-40 at the surface against data from the Mackenzie and Mississippi River basins (Betts et al. 2003a,b). Figure 7 shows these basins for the Americas: the red-numbered quadrilaterals are the model approximation to the river basins shown in brown (the blue numbers correspond to archive points where there are flux tower observations for comparison). For this paper, we choose three river subbasins:

- 42: Madeira: a southwestern subbasin of the Amazon,
- 28: Arkansas–Red: a southwestern subbasin of the Mississippi, and
- 39: Athabasca: a southeastern subbasin of the Mackenzie.

From the hourly time series, we computed daily averages for the 30-yr period from January 1972 to May 2002, some 11,000 days, as well as the diurnal range of temperature and relative humidity. In addition to the basic state variables and fluxes, we also have the model cloud cover.

Diurnal and seasonal cycles of ERA-40 for Madeira River basin compared with LBA Rondonia pasture site for 1999. First we compare in Fig. 8 the diurnal and seasonal cycles of ERA-40 for the Madeira River basin with the LBA pasture site in Rondonia, Brazil (see Betts et al. 2002), within this basin. Comparing the Rondonia point data and the ERA-40 Madeira basin mean is hardly a fair comparison, but we see broadly similar diurnal and seasonal structure, with the much larger-scale basin mean having a reduced seasonal range. The four panels for the Madeira basin and Rondonia pasture, respectively, in Fig. 8 show the mean diurnal cycle of near-surface temperature, mixing ratio, equivalent potential temperature, and P_{LCL}, the pressure height to the LCL. The colors from blue to red show the transition in the mean diurnal cycle from the rainy season through to the dry season in August, averaged for the months shown. Note that the mean temperature changes little, but the amplitude of the diurnal cycle of temperature increases sharply from the rainy to the dry season as the outgoing LW_{net} increases (not shown). This is associated with the drier (and less cloudy) atmosphere. The mean LCL height P_{LCL} (a good approximation to mean cloud base in the daytime) grows from the rainy to dry season, and the ML gets warmer and drier.

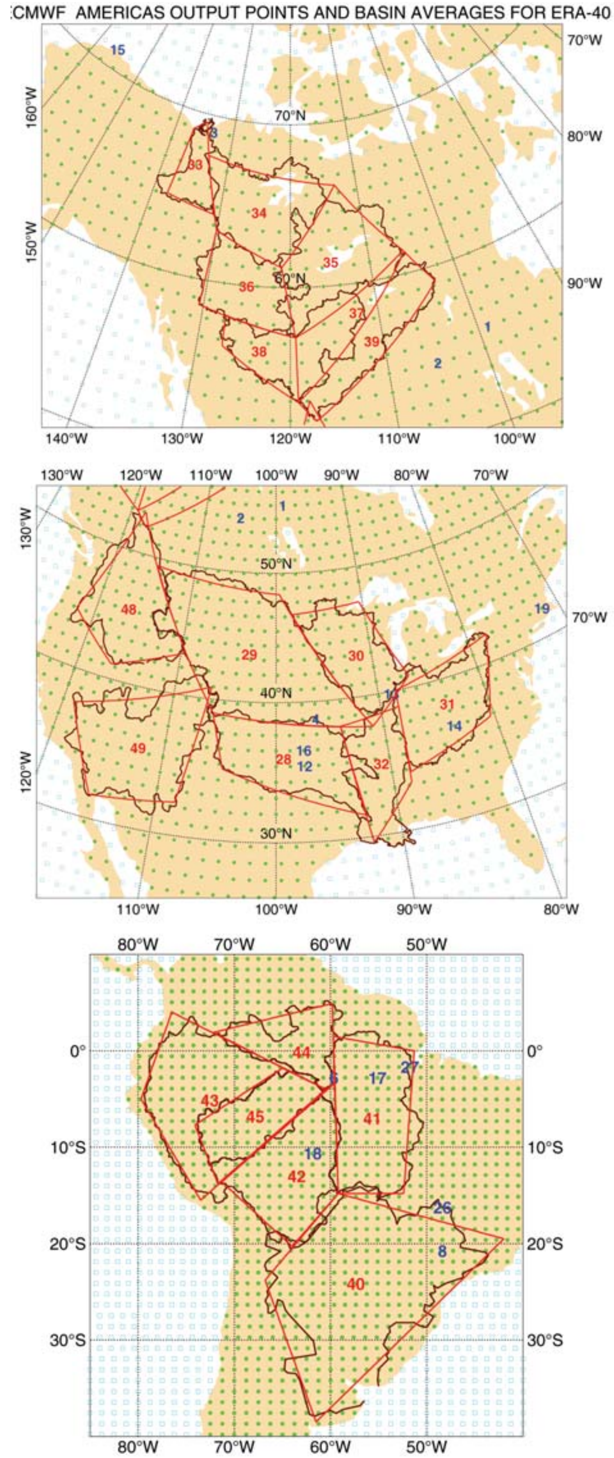

Fig. 7. ERA-40 basin and point hourly archive for the Americas. The red-numbered quadrilaterals are the model approximations to the river basins shown in brown; the blue numbers correspond to archive points, where there are flux tower observations for comparison.

Coupling of soil moisture index, cloud-base height, and evaporative fraction. These daily mean data from ERA-40 from 1972 to 2002 can be used to explore the link

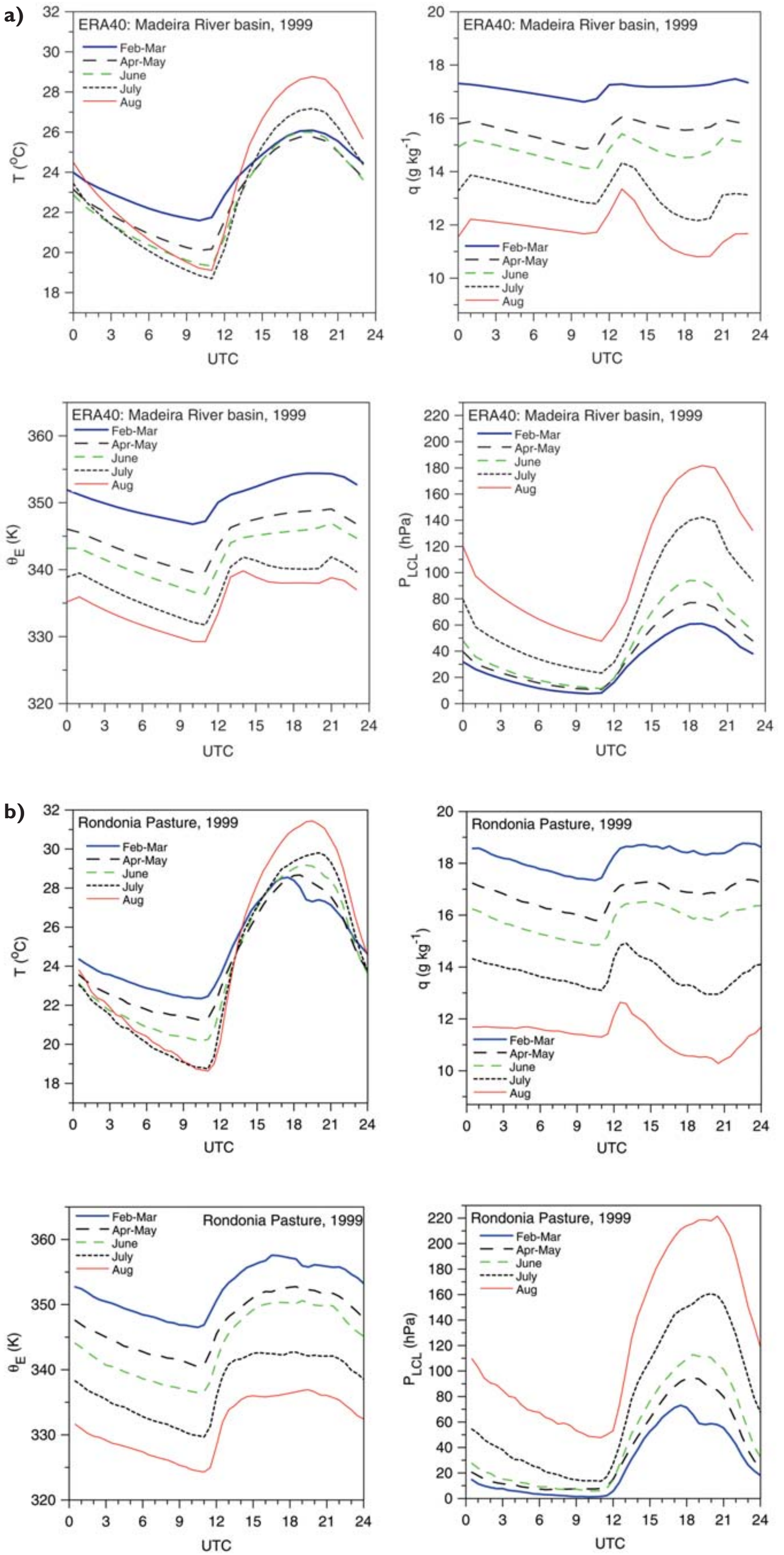

between soil moisture, cloud-base height, and evaporative fraction [defined as $\lambda E/(\lambda E + H)$]. The upper panels of Fig. 9 for the Madeira basin are P_{LCL} and evaporative fraction as a function of SMI for the first 0–7-cm soil layer, partitioned into two ranges of R_{net}, $110 < R_{net} < 150$ W m^{-2} and $150 < R_{net} < 190$ W m^{-2}. We see that the mean cloud-base height increases over drier soils and with larger surface R_{net}, while evaporative fraction increases with soil moisture, and decreases with R_{net}. The lower panels of Fig. 9 average the daily points into 0.1 range bins of SMI, and add the summer data [June–July–August (JJA)] for the Arkansas–Red and Athabasca basins. Again we have split the data into the same two ranges of R_{net} and labeled the curves with the midrange values of 130 and 170 W m^{-2}; in addition, we have added the standard deviation for the lower R_{net} range to show how tight the distributions are. Within the error bars, the Arkansas–Red and Madeira basins form a single distribution, even though soil moisture is much lower in the Arkansas–Red basin. The tropical forest and this southern basin of the Mississippi have similar

Fig. 8. Comparison of the seasonal change of the mean diurnal cycle of near-surface temperature, mixing ratio, equivalent potential temperature, and P_{LCL} for ERA-40 for the Madeira River basin, with the LBA pasture site in Rondonia.

unstressed vegetative resistance (which depends on the model vegetation type), of order 250 s m^{-1}. However, the Athabasca basin, which is more than 90% boreal forest (see Betts et al. 2003b), has a much higher unstressed vegetative resistance in the model (500 s m^{-1}), and has correspondingly higher cloud bases and a lower evaporative fraction than the other two basins for the same SMI.

Madeira basin for July and November. There are considerable differences in the coupling at the surface between the dry and rainy seasons. This is illustrated by 2 months—July for the dry season, when the solar zenith angle for this basin (south of the equator) is greater, and November, after the onset of the rainy season, when the solar zenith angle is smaller. The upper panels of Fig. 10 show for the 2 months the terms in the daily surface energy balance as a function of mean cloud-base P_{LCL}, specifically, the radiation fluxes, SW_{net}, R_{net}, LW_{net}, the sensible heat H, and latent heat λE. The global model sign convention has been kept for the terms, and the left- and right-hand scales are the same except in sign, so that visually $R_{net} = -(\lambda E + H)$ (neglecting the small ground storage), and $SW_{net} = R_{net} - LW_{net}$. The lower panels show just the radiative fluxes as a function of total cloud cover in the model. Not shown is the fact that cloud cover decreases as the P_{LCL} gets deeper and the ML gets drier. In the dry season in July, the range of P_{LCL} is larger than in November, when the ML is closer to saturation and the total cloud cover is, on average, higher. However, the incoming SW_{net} is higher in November than July, for either the same cloud base or cloud cover, because of the smaller zenith angle. The upper-left panel shows the same linear distribution of H with P_{LCL}, seen in Fig. 5, but note that LW_{net} against P_{LCL} has a similar slope and an even tighter distribution. Because both SW_{net} and ($-LW_{net}$) both increase with P_{LCL}, R_{net} increases rather weakly with P_{LCL}, and because $-H$ increases with P_{LCL}, we see that $-\lambda E$, regarded as the residual $R_{net} + H$, is almost independent of P_{LCL}. Note that the slope of $-H$ with P_{LCL} is greater in the rainy season, but that of LW_{net} against P_{LCL} is the same.

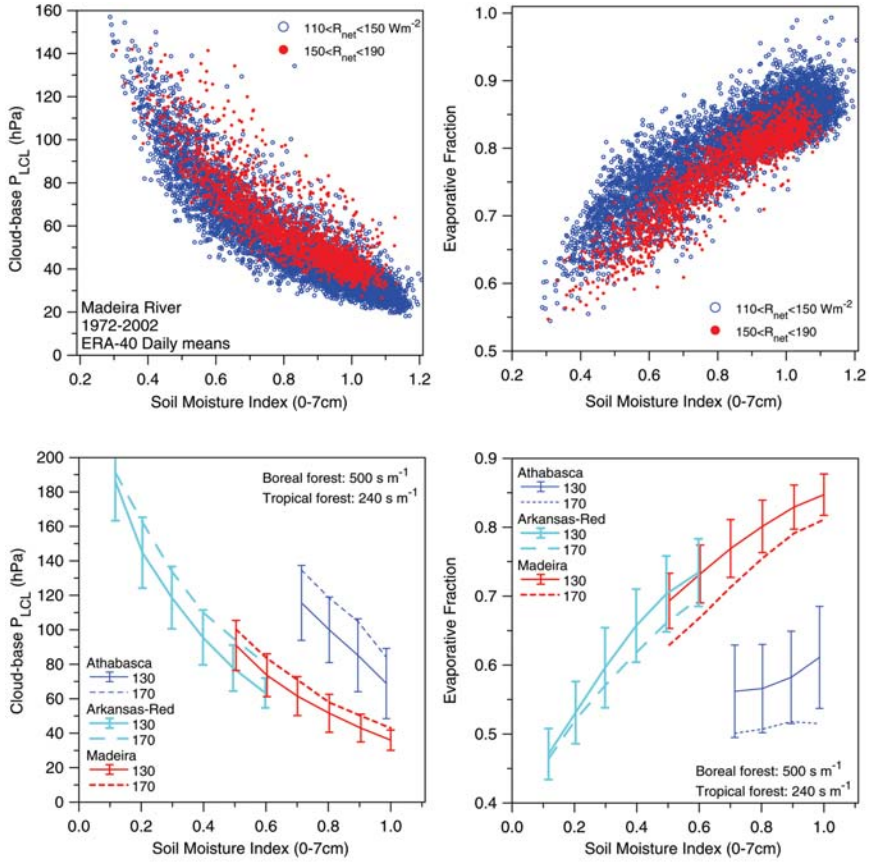

FIG. 9. Scatterplots for the (top) Madeira basin of P_{LCL} and evaporative fraction, partitioned into two ranges of R_{net}, as a function of SMI for the first 0–7-cm soil layer, and (bottom) P_{LCL} and evaporative fraction averaged in SMI bins, and partitioned into two ranges of R_{net}, for the Madeira, Athabasca, and Red–Arkansas basins.

Figure 11 shows the surface LW_{net} as a function of the soil moisture index (0–7-cm layer), cloud base, total cloud cover, and diurnal range of radiometric skin temperature. The points for July and November merge to a single distribution for three of the plots, against SMI, P_{LCL}, and diurnal temperature range. The other months of the year fall in between, filling in the same distribution. In the total cloud cover plot the distributions for the 2 months just separate, probably because the vertical distribution of cloud cover is different in the rainy season, when there is much more high cloud (not shown). The right-hand panels mean that the relationship between diurnal temperature range and LW_{net} is also tight in the model, and we shall return to this later. All five of the axis variables in Fig. 11 are coupled to each other over land in the

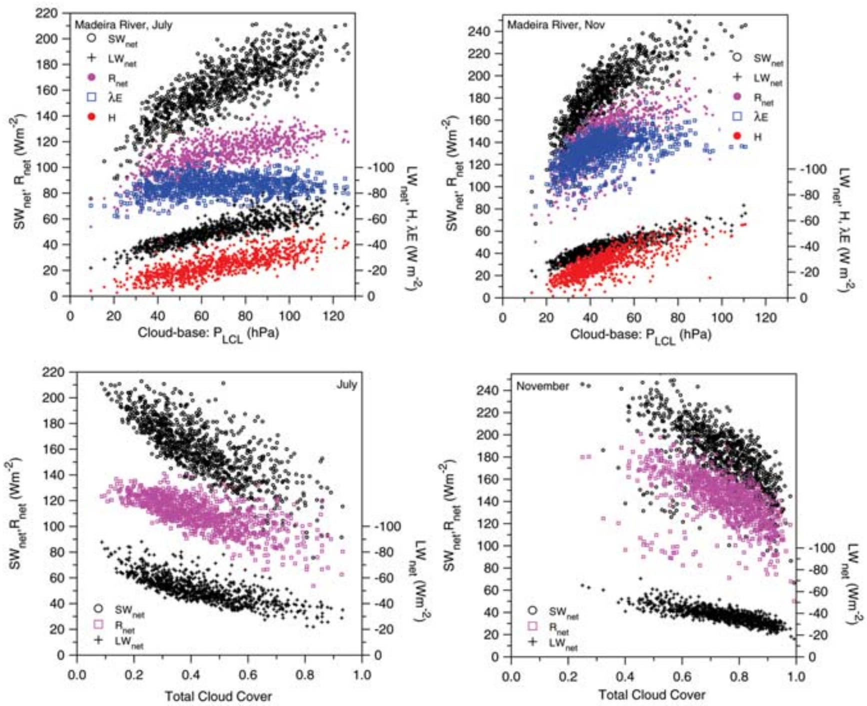

FIG. 10. (top) Surface energy balance terms SW_{net}, R_{net}, LW_{net}, sensible heat *H,* and latent heat λE as a function of mean cloud-base P_{LCL} for Jul and Nov, and (bottom) radiation fluxes as a function of total cloud cover.

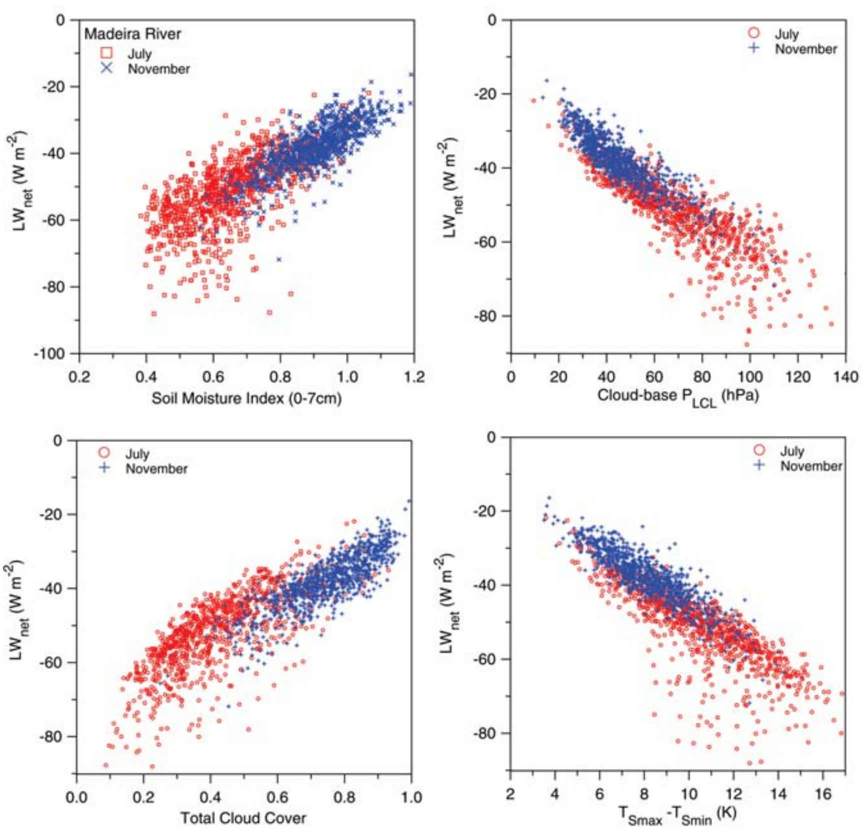

FIG. 11. Surface LW_{net} as a function of soil moisture index (0–7-cm layer), cloud base, total cloud cover, and the diurnal range of radiometric skin temperature for Jul and Nov for the Madeira River basin.

ERA-40 model. In physical terms this coupling makes sense; shallower, cloudier BLs occur over moist soils, and they have smaller outgoing net longwave radiation and a reduced diurnal temperature range. We cannot clearly identify cause and effect (and the other terms in the surface energy budget in the following figures are also coupled), but it is significant that the couplings shown on the right of Fig. 11 are the tightest, even if all months of the year are included (not shown).

Figure 12 shows SW_{net} against LW_{net}, cloud base, total cloud cover, and sensible heat flux. The first three plots show two distinct distributions for July and November (the other months fall in between, not shown). The coupling (top left) between SW_{net} and LW_{net} is very tight in each month, but the lower-left panel shows that the SW_{net} dependency on cloud cover is different in each month. In November, the smaller zenith angle and the higher cloud cover have partly compensating effects on SW_{net}, while the higher cloud cover and lower cloud base reduce LW_{net}. The upper-right panel shows that the variation with P_{LCL} is quite different for the 2 months (contrast the corresponding panel of Fig. 11 for LW_{net}). The lower-right panel shows that, remarkably, the coupling between SW_{net} and the surface sensible heat flux is similar for both months (and for all months of the year, not shown).

Figure 13 shows sensible heat flux against the diurnal range of skin temperature (DTsR), maximum skin temperature, cloud base, and SW_{net}. In the upper left, the reduced DTsR in November for the same H is the result of more rain producing greater surface evaporation (both from increased soil moisture and, at times, a wet canopy). The lower-left panel shows that the distributions in the 2 months correspond to quite different heating rates of the layer of mean thickness P_{LCL}. In July the surface heat flux H warms this layer by 3 K day^{-1}, which closely balances the radiative cooling rate (as in the equilibrium solutions of Betts 2000; Betts et al. 2004). However, in November, the surface flux heats the much shallower layer at about 6 K day^{-1}, and it is additional evaporative cooling by falling precipitation (as well as some radiative cooling) that probably maintains the boundary layer temperature. Note that evaporation of precipitation below cloud base increases the surface sensible heat flux, while evaporation of precipitation off a wet canopy increases the surface latent heat flux; these are opposite effects in the surface energy balance partition. The right-hand panels show that H is closely

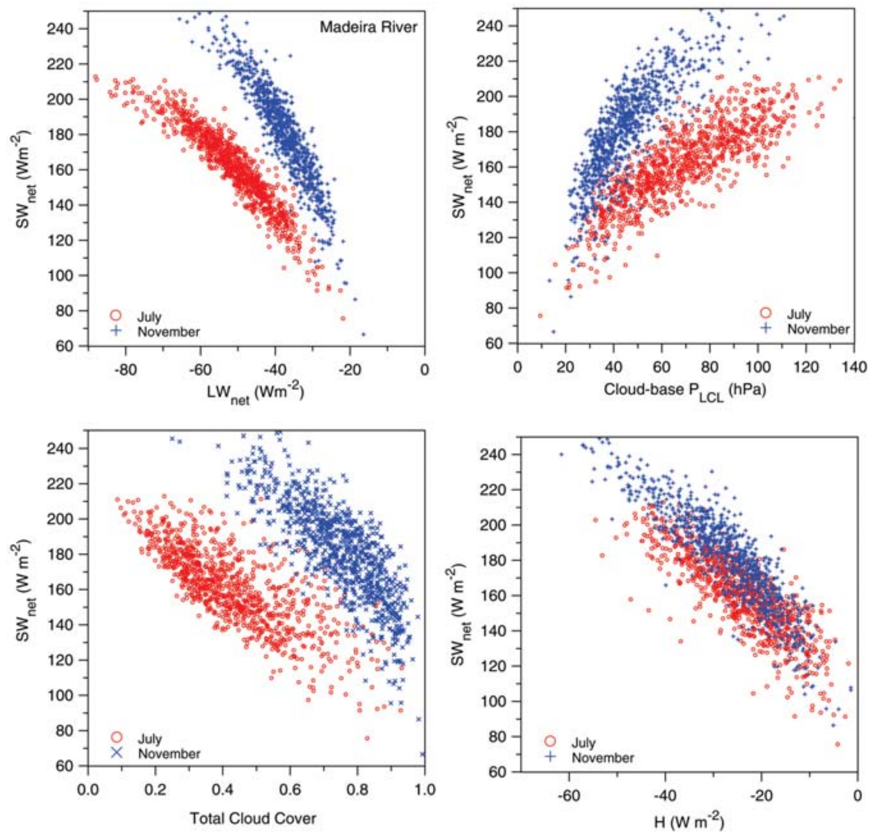

FIG. 12. As in Fig. 11, but for SW_{net} against LW_{net}, cloud base, total cloud cover, and sensible heat flux.

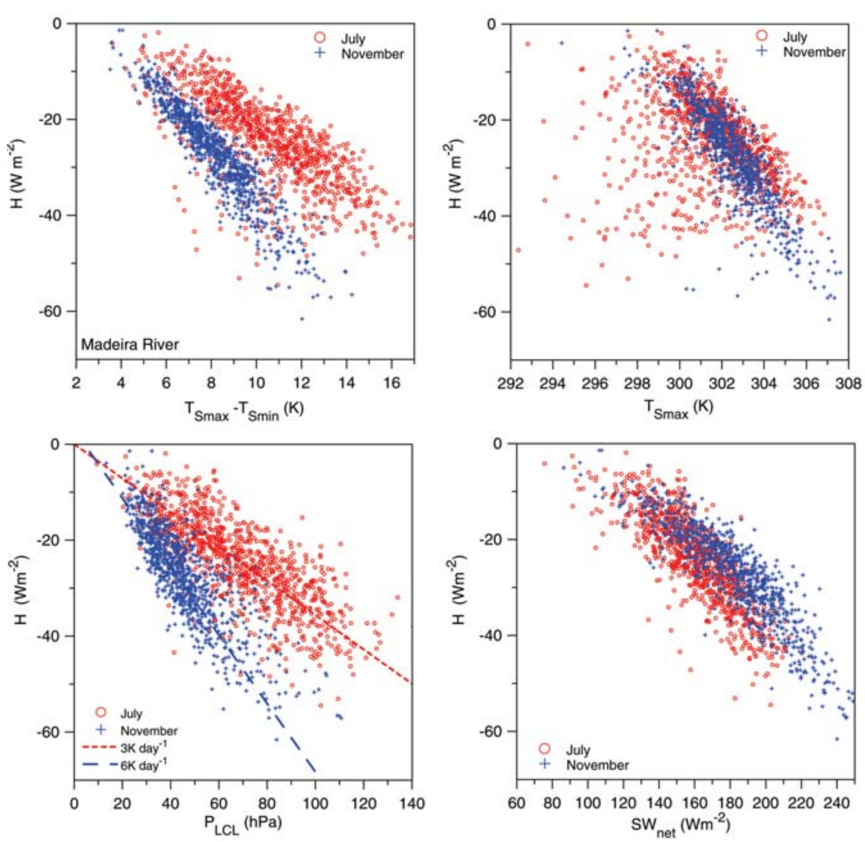

FIG. 13. As in Fig. 11, but for sensible heat flux against diurnal range of skin temperature, maximum skin temperature, cloud base, and SW_{net}.

coupled to the maximum skin temperature (upper right), and we repeat the coupling to SW_{net}. The skin temperature responds to the daytime shortwave (SW) radiation, and H to the skin temperature. We see that H is coupled to several processes—the SW forcing at the surface, and the radiative and evaporative cooling of the layer below mean cloud base—and all of these processes are coupled to the cloud fields.

Figure 14 shows latent heat flux λE and sensible heat flux H against the soil moisture index (top) and R_{net} (bottom). It is the sensible heat flux (top right) rather than the evaporation (top left) that can be seen to vary with SMI (but the variation differs for the 2 months). SMI controls P_{LCL} quite directly (see Fig. 9), but in the rainy season H is increased by additional BL cooling processes (Fig. 13). The lower panels show the links between the fluxes and R_{net}. Latent heat λE has more variation with R_{net} in November, representative of the rainy season months from November to April, while July is representative of the much weaker variation of λE with R_{net} in the dry season. Contrast (lower right) the two branches for H as a function of R_{net} with the corresponding lower-right panel of the previous Fig. 13 against SW_{net}.

Priestley–Taylor ratio. Figures 10–14 explore the interrelationship on the daily time scale between many parameters: the surface sensible and latent heat fluxes, soil moisture index, total cloud cover, height of cloud base, and net shortwave and longwave fluxes. What do these relationships mean for evaporation in terms of the classic Priestley–Taylor ratio, which may be defined as

$$\text{Priestley–Taylor ratio} = \mathrm{EF}(1+\varepsilon)/\varepsilon, \qquad (1)$$

where $\mathrm{EF} = \lambda E/(R_{net} - G) = \lambda E/(\lambda E + H)$? The thermodynamic coefficient $\varepsilon = (\lambda/C_p)dQ_s/dT$ is related to the change of saturation mixing ratio with temperature (following Betts 1994, we define this at the LCL temperature).

Figure 15 shows the scatterplot of the Priestley–Taylor ratio for July and November for the Madeira basin against SMI and R_{net}. We see the now-familiar two separate branches for July and November. Both show higher values of the Priestley–Taylor ratio for higher soil water and lower R_{net}, with upper values near 1.26, consistent with many previous analyses. The 20% variation in the Priestley–Taylor ratio corresponds to a 20 W m^{-2} change in the partition of the surface energy budget. While an error of 10%–20% might be acceptable in surface evaporation for some more traditional hydrological purposes, for climate interactions overland this is a large error. This means that we must both understand the coupling with the cloud field and BL structure shown in figures 10–14, and also validate the relationships shown in the model against observations.

LW coupling for other basins. The coupling of the LW_{net} to total cloud cover and P_{LCL}, shown in Fig. 11, is quite general. Figure 16 shows for the three Americas' basins the mean variation of LW_{net} against total cloud cover, binned in 0.2 bin ranges, and against cloud-base P_{LCL} (in 20-hPa bins).

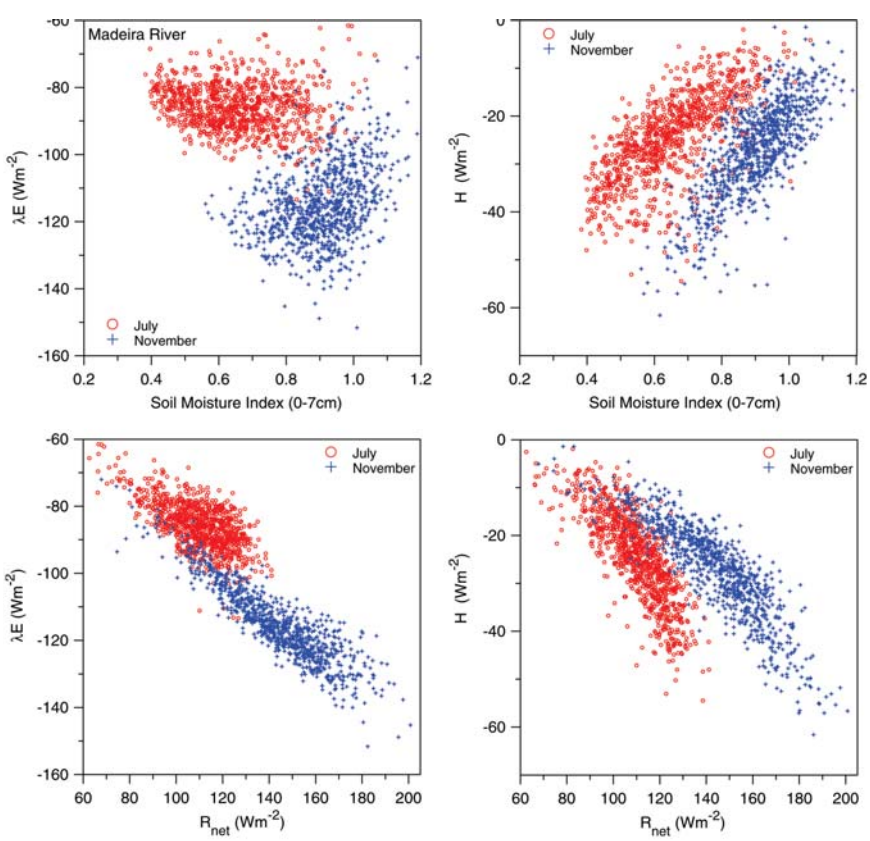

FIG. 14. As in Fig. 11, but for latent heat flux λE and sensible heat flux H against (top) soil moisture index and (bottom) R_{net}.

The Madeira basin daily data covers the full 30 yr, while the Athabasca and Red–Arkansas basin data are for summer (JJA) only. In the left-hand plot against total cloud cover, the curve for the Madeira basin is above the mid-latitude basins, but this is consistent with it having a 50-hPa mean lower cloud base, and a moister BL. On the right, the Red–Arkansas is below the other two, but this too is consistent with it having a lower total cloud cover (about 0.25 less than the Athabasca). There is a only a small shift of the distribution, for the same P_{LCL} and cloud cover, to larger outgoing LW at high latitudes as the emissivity of the overlying atmosphere decreases. This tight coupling between LW_{net} and P_{LCL} is undoubtedly an important land surface feedback, as noted by Schär et al. (1999). Over wet soils, the cloud base is lower and the outgoing longwave radiation is decreased.

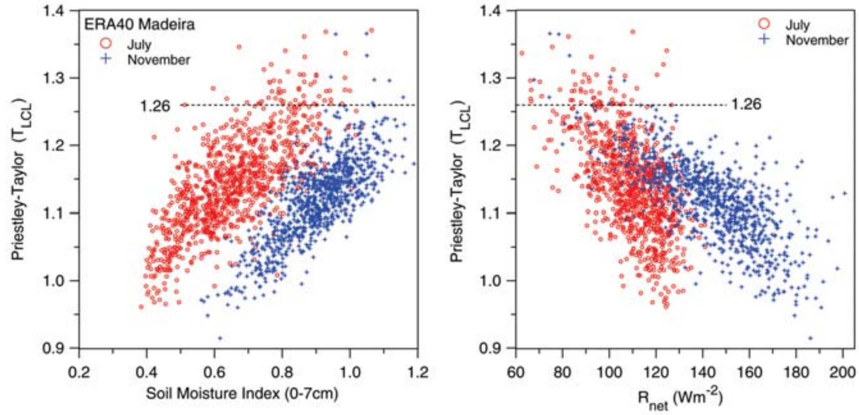

Fig. 15. Priestley–Taylor ratio for Jul and Nov for the Madeira basin plotted against soil moisture index and R_{net}.

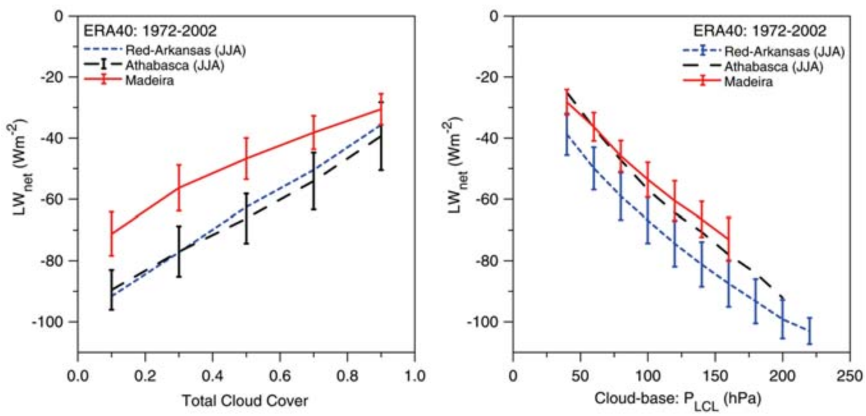

Fig. 16. Mean variation of LW_{net} against total cloud cover and cloud-base P_{LCL} for the three Americas basins.

Diurnal cycle. The last part of this analysis addresses the diurnal cycle of temperature and relative humidity (RH), both important aspects of the climate system. Figure 17 for the Madeira basin shows maximum and minimum skin temperatures T_{Smax} and T_{Smin}, respectively, and the difference DTsR (right-hand scale) plotted against LW_{net}. Note that DTsR is coupled quite tightly to LW_{net}, as shown previously in Fig. 11; the width of the distribution is less than that of either T_{Smax} or T_{Smin}. Figure 18 (left panel) plots the diurnal range of the 2-m temperature (DT2R), an important climate variable, against LW_{net}. Also plotted is the temperature change computed from LW_{net} and the slope of the Planck function

$$\Delta T_{Planck} = -LW_{net}/4\sigma T^3. \tag{2}$$

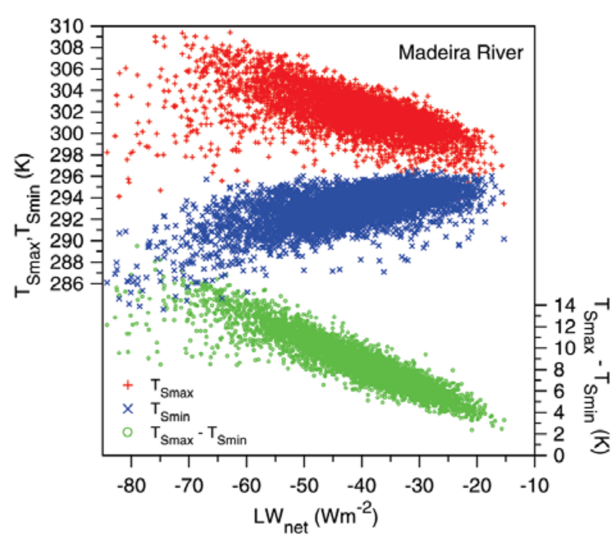

Fig. 17. Maximum and minimum skin temperatures T_{Smax} and T_{Smin}, respectively, and the diurnal range of skin temperature (right-hand scale) plotted against LW_{net} for the Madeira basin.

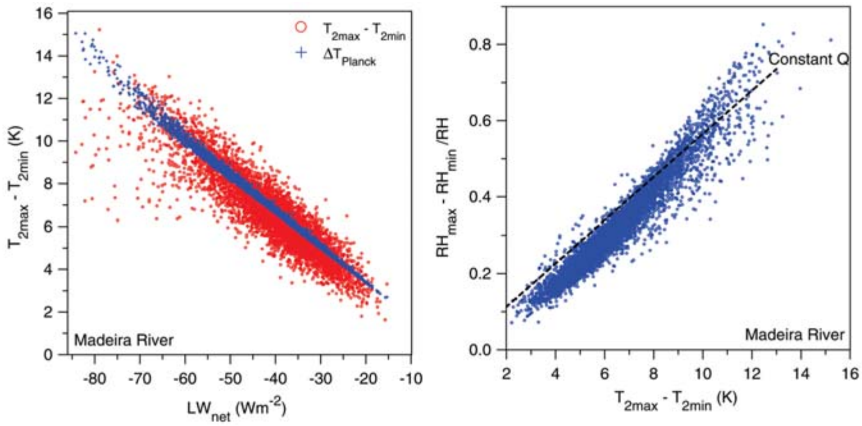

FIG. 18. Diurnal range of the 2-m temperature ΔT_{Planck} [see Eq. (2)] plotted against (left) LW_{net} and (right) the coupling between the diurnal range of RH, scaled by the diurnal mean of RH, and the diurnal temperature range for the Madeira basin.

Not only is diurnal range of temperature tightly related to the LW_{net}, but ΔT_{Planck} gives a good estimate of DT2R in the model in the Tropics. At higher latitudes, the ratio DT2R/ΔT_{Planck} decreases to 0.8 (not shown). The right panel of Fig. 18 shows the tight coupling between the diurnal temperature range and the diurnal range of RH (scaled by the diurnal mean of RH). This is largely a result of the fact that the diurnal range of mixing ratio Q is small (see Fig. 8), because the large surface evaporation is transported up through the cloud base. The dotted line is the coupling for constant Q. Except for large values of DT2R, which correspond to deep, dry daytime BLs, the points for the Madeira basin lie below the dotted line, because at the temperature minimum, the surface air saturates and $Q_s(T_{min})$ is less than $Q(T_{max})$. Drier basins, such as the Red–Arkansas (not shown), show a small upward shift of the distribution relative to the dashed constant Q line.

CONCLUSIONS. Modeling climate and climate change over land depends critically on the coupling between the cloud and radiation fields, the surface partition of sensible and latent heat, soil water (and other constraints on evaporative resistance), and the boundary layer (as well as subsurface hydrologic processes that we have not addressed here); so we have tried to map out some of these links in the ECMWF model at the time of ERA-40. The first section addressed evaporation–precipitation feedback in seasonal forecasts for the Northern Hemisphere summer, initialized with idealized "wet" and "dry" soils for vegetated areas. We showed that away from the monsoon regions, the ERA-40 model has a large evaporation–precipitation feedback over the continents, and the memory of initial soil moisture is longest at high northern latitudes. We might well ask whether this strong feedback is correct, because other work (Koster et al. 2002) shows that this feedback differs widely in different models, presumably because each model differs in the way it parameterizes the many physical processes we have discussed. We then showed that the change in the surface energy budget over dry and wet soils is consistent with a shift of the mean subcloud-layer equilibrium, and is also broadly consistent with an idealized (diurnally averaged) equilibrium model for the boundary layer.

The second section addressed the coupling of the soil moisture, cloud base, cloud cover, radiation fields, sensible and latent heat fluxes, and diurnal cycle, using 30 yr of daily river basin data from ERA-40 for three basins in the Americas: the Madeira, Red–Arkansas, and Athabasca. It is clear that the tight coupling to cloud processes plays an essential role in the BL equilibrium, and that although the model fully resolves the diurnal cycle and has a prognostic interactive cloud field, the transitions in the BL climate over land can nonetheless be mapped with remarkable precision by the daily mean state and daily flux averages.

Mean cloud-base height increases over drier soils with larger surface R_{net}, while evaporative fraction increases with soil moisture and decreases with R_{net}. The differences in the coupling at the surface between the dry season and the rainy season were illustrated for the Madeira basin by selecting 2 months: July for the dry season, and November, after the onset of the rainy season. Both surface LW_{net} and H have similar linear slopes when plotted against P_{LCL} in the dry season, with LW_{net} having a rather tighter distribution. More generally, it is clear that model data such as that from ERA-40 can be used to understand the coupling of processes at the land surface. Soil moisture, cloud base, cloud cover, radiation fields, and evaporative fraction are indeed coupled quite tightly on daily average time scales. The longwave flux control by cloud-base height and cloud cover is particularly tight across all basins, and is, thus, an important feedback between the cloud field and the surface energy budget, as noted by Schär et al. (1999). The sensible heat flux is coupled to cloud-base height and cooling processes (radiative and precipitation evaporation) in the subcloud layer, as well as directly to the shortwave flux. Evaporation can be regarded as being "controlled" somewhat indirectly by the dependence of net radiation on cloud cover and cloud base, and sensible heat flux on subcloud-layer processes. It appears that evaporation of precipitation below cloud base and off wet canopies plays opposite roles in the partition of the surface energy balance into latent and sensible heat. The diurnal cycle of temperature is tightly coupled to the net longwave flux, which, in turn, is controlled by mean cloud-base height and cloud cover; while the diurnal cycle of relative humidity and temperature are closely related, because the diurnal variation of the mixing ratio is small.

What we have shown is that there are strong feedbacks on the daily time scale between the cloud field (through cloud base, cloud cover, and diabatic processes within the BL) and the surface energy budget, and the partition into sensible and latent heat. This means that cloud and boundary layer processes and the land surface components of a model must be evaluated as a tightly coupled system, not as independent components. Indeed, this analysis provides a framework for comparing global models with each other, and for validating them against climate observations. (This is a large task, which we have barely begun.) It suggests that relative humidity, cloud base, and cloud cover need to be measured along with the longwave and shortwave radiation fields as part of a climate measuring system (which traditionally has only measured temperature, precipitation, and solar radiation). In addition, the importance of so many coupled processes at the land surface presents a major validation challenge for climate models that use interchangeable plug-in modules for the different physical processes. The basic land surface feedback may change every time a module is changed, and so each combination must be carefully assessed.

ACKNOWLEDGMENTS. This research has been supported by NASA Grant NAG5-11578 and by NSF Grant ATM-9988618. Most of the work discussed here is based on collaboration with colleagues at ECMWF.

It was an honor and a delight to give the Robert E. Horton 2004 lecture. I have an advantage being in Vermont, away from institutional stresses, to have time to think. For this I would like to thank the National Science Foundation (NSF), National Aeronautics and Space Administration (NASA), and National Oceanic and Atmospheric Administration (NOAA) for funding my work, and all of you that have supported and collaborated with me over the years. I would also especially like to thank my colleagues at the European Centre for Medium-Range Weather Forecasts (ECMWF), particularly Anton Beljaars, Pedro Viterbo, and Martin Miller, for two decades of extensive collaboration. Almost everything in this lecture is based on their foresight in model development, and I strongly recommend to the next generation that you find opportunities to visit and work there, to see what can be achieved with a clear focus and good scientific management. Last, my thanks to John Ball in Vermont for 15 years of patient data processing.

REFERENCES

Beljaars, A. C. M., and A. K. Betts, 1993: Validation of the boundary layer representation in the ECMWF model. Vol. II, *ECMWF Seminar Proc. on the Validation of Models over Europe,* Shinfield Park, Reading, United Kingdom, 159–195.

——, P. Viterbo, M. J. Miller, and A. K. Betts, 1996: The anomalous rainfall over the United States during July 1993: Sensitivity to land surface parameterization and soil moisture anomalies. *Mon. Wea. Rev.,* **124**, 362–383.

Betts, A. K., 1973: Non-precipitating convection and its parameterization. *Quart. J. Roy. Meteor. Soc.,* **99**, 178–196.

——, 1994: Relation between equilibrium evaporation and the saturation pressure budget. *Bound.-Layer Meteor.,* **71**, 235–245.

——, 2000: Idealized model for equilibrium boundary layer over land. *J. Hydrometeor.,* **1**, 507–523.

——, and J. H. Ball, 1994: Budget analysis of FIFE-1987 sonde data. *J. Geophys. Res.,* **99**, 3655–3666.

——, and ——, 1995: The FIFE surface diurnal cycle climate. *J. Geophys. Res.,* **100**, 25 679–25 693.

——, ——, and A. C. M. Beljaars, 1993: Comparison between the land surface response of the European Centre model and the FIFE-1987 data. *Quart. J. Roy. Meteor. Soc.,* **119**, 975–1001.

——, ——, ——, M. J. Miller, and P. Viterbo, 1996: The land-surface-atmosphere interaction: A review based on observational and global modeling perspectives. *J. Geophys. Res.,* **101**, 7209–7225.

——, J. Fuentes, M. Garstang, and J. H. Ball, 2002: Surface diurnal cycle and boundary layer structure over Rondonia during the rainy season. *J. Geophys. Res.,* **107**, 8065, doi: 10.1029/2001JD000356.

——, J. H. Ball, M. Bosilovich, P. Viterbo, Y.-C. Zhang, and W. B. Rossow, 2003a: Intercomparison of water and energy budgets for five Mississippi subbasins between ECMWF reanalysis (ERA-40) and NASA Data Assimilation Office fvGCM for 1990–1999. *J.*

Geophys. Res., **108** (D16), 8618, doi:10.1029/2002JD003127.
——, ——, and P. Viterbo, 2003b: Evaluation of the ERA-40 surface water budget and surface temperature for the Mackenzie River basin. *J. Hydrometeor.,* **4**, 1194–1211.
——, B. Helliker, and J. Berry, 2004: Coupling between CO_2, water vapor, temperature and radon and their fluxes in an idealized equilibrium boundary layer over land. *J. Geophys. Res.,* **109** (D18103), doi:10.1029/2003JD004420.
Koster, R. D., P. A. Dirmeyer, A. N. Hahmann, R. Ijpelaar, L. Tyahla, P. Cox, and M. J. Suarez, 2002: Comparing the degree of land–atmosphere interaction in four atmospheric general circulation models. *J. Hydrometeor.,* **3**, 363–375.
Raupach, M., 2000: Equilibrium evaporation and the convective boundary layer. *Bound.-Layer Meteor.,* **96**, 107–141.
——, 2001: Combination theory and equilibrium evaporation. *Quart. J. Roy. Meteor. Soc.,* **127**, 1149–1181.
Schär, C., D. Lüthi, U. Beyerle, and E. Heise, 1999: The soil–precipitation feedback: A process study with a regional climate model. *J. Climate,* **12**, 722–741.
Van den Hurk, B. J. J. M., P. Viterbo, A. C. M. Beljaars, and A. K. Betts, 2000: Offline validation of the ERA40 surface scheme. ECMWF Tech. Memo. 295, 43 pp. [Available online at www.ecmwf.int/publications/library/ecpublications/_pdf/tm/001-300/tm295.pdf.]
Viterbo, P., and A. C. M. Beljaars, 1995: An improved land surface parameterization in the ECMWF model and its validation. *J. Climate,* **8**, 2716–2748.